Supplementary information

Development of high-performance deicing coatings through engineered weak interfacial domains

Zhile Han [a b], Xinchun Tian [a b d e]*, Yipeng Peng[c]*, Linchuan Tian [f], Jingyi Tu [f], Jiangnan Liu [a b], Wei Sun [a b], Zhaowen Xu [a b], Dong Wang [a b], Zhuang Ma [a b d e g]

[a] School of Materials Science and Engineering, Beijing Institute of Technology, Beijing, 100081, China
[b] Tangshan Research Institute, Beijing Institute of Technology, Tangshan, 063000, China
[c] Department of Mechanics and Engineering Science, School of Physics, Nanjing University of Science and Technology, Jiangsu, 210094, China
[d] National Key Laboratory of Science and Technology on Material under Shock and Impact, Beijing, 100081, China
[e] Materials Intelligent Innovation laboratory (MIIL), Beijing Institute of Technology, Zhuhai, 519088, China
[f] School of Aeronautics and Astronautics, Shanghai Jiao Tong University, Shanghai, 200240, China
[g] Beijing Institute of Technology Chongqing Innovation Center, Chongqing, 401120, China

*Corresponding Author (xctian@bit.edu.cn; yppeng@njust.edu.cn)

S1 Supplementary methods

S1.1 Preparation of the solely surface-modified coatings

For surface hydrophobicization, chemical vapor deposition (CVD) was employed. Specifically, 0.3 mL of $C_{10}M$ was placed in a beaker alongside the WPU coating (100 μm thickness) within a sealed reaction vessel. The vessel was evacuated and maintained at 40 °C for 3 h. The beaker was then removed, and the vessel was re-evacuated and reacted again at 40 °C for 12 h. Finally, the coating was dried at 80 °C for 10 h to obtain the hydrophobic-modified surface.

S1.2 Ice adhesion force measurement

Ice adhesion force was measured using a custom-built apparatus comprising a temperature-controlled environmental chamber, a force gauge (Imada ZP-50N), and a syringe pump (SPLab01, DK Infusetek Technology Co.) programmed to advance the force gauge at a constant rate of 0.1 mm/s. Except for cases where temperature is specifically mentioned, most tests were conducted in a sealed chamber under stable environmental conditions (–15°C, 80% relative humidity) to minimize thermal fluctuations. Ice samples were prepared using rectangular plastic molds. The inner cavity of each mold had a fixed width of 1 cm and a depth of 3 cm, with lengths varying from 1 cm to 13 cm. The mold walls were approximately 2 mm thick, so the outer dimensions of the molds were slightly larger. During preparation, molds were placed on the coating surface and filled with deionized water to a height of 1 cm within the cavity. After complete freezing, the resulting ice samples had a fixed cross-section of 1 cm × 1 cm (width × height) and a variable length ranging from 1 cm to 13 cm. The customized probe tip of the force gauge was positioned 1 mm above the coating surface and advanced gradually until contact with the ice sample was made. The ice adhesion strength (τ_{ice}) was calculated by dividing the maximum dislodgement force by the ice-coating contact area (width × length), and the interfacial toughness (Γ_{ice}) was characterized using ice samples with a fixed height (1 cm) but variable length (1–13 cm).

S1.3 Interfacial toughness (Γ_{ice}) calculation

Γ_{ice} was calculated according to reference [1]. The force per unit width (F) required to dislodge ice from the coating surface was measured as a function of ice length (L). For each coating system, the F–L relationship was analyzed in two distinct regimes: for $L \leq L_{cr}$, a linear fit was applied to determine the slope; for $L \geq L_{cr}$, a horizontal linear fit (with slope k = 0) was used to obtain the intercept.

S1.4 Durability test

The durability of the coating was evaluated under five conditions: for chemical resistance, coated samples were immersed in acidic and alkaline aqueous solutions for 10 days each; for water impact exposure, the coating was subjected to a water jet at 0.07 MPa and 7.2 L/min for 30 minutes; for salt spray testing, samples underwent continuous salt spray exposure in a controlled chamber for 14 days; and for abrasion resistance, 400 g of silica sand particles were released from a funnel 1 m above the sample and collided with the coating surface fixed at a 45° angle.

S1.5 Additional coating property characterizations

The mechanical properties of the coating were evaluated in accordance with ASTM D412 using 1 mm thick samples. Tensile tests were performed on a tensile shear strength tester (HAK-3516D, Shenzhen Kexing Precision Instrument Co., Ltd.) at a crosshead speed of 100 mm/min.

Coating thickness and fracture surface morphology were characterized using a scanning electron microscope (SU 8600, Hitachi, Japan).

Static and dynamic contact angles were measured using a video-based optical contact angle analyzer (SDC-200S, SINDIN, China). Static contact angle measurements were conducted by depositing 5 μL water droplets onto flat rectangular substrates [2]. For dynamic contact angle measurements, a water droplet with an initial volume of 6 μL was dynamically expanded and contracted at a rate of 0.1 μL/s using an automated syringe pump. The advancing angle was

recorded when the contact line advanced without further increase in angle, while the receding angle was measured when droplet retraction initiated.

FTIR-ATR spectra were acquired using a Nicolet iS50R spectrometer (Thermo Fisher Scientific, USA) over the range of 4000–400 cm^{-1}.

Coating adhesion to aluminum alloy substrates was assessed following ASTM D3359-17 and ASTM C633 standards. For ASTM C633 tests, cylindrical substrates (Ø25.4 mm × 1 mm) with 1.0 mm thick coatings were evaluated using a universal tensile machine (WDW-E100D, Jinan Shijin Group Co., Ltd.). The thickness of coatings was 1.0 mm.

Shore hardness was measured according to ASTM D2240, and optical transmittance spectra were obtained at room temperature using a UV-Vis spectrophotometer (Lambda 1050+, PerkinElmer).

S1.6 Phase field simulation

A finite-strain variational phase-field fracture formulation is employed to investigate how weak interfacial domains affect shear transfer and interfacial crack nucleation during ice detachment (**Figure 6a-b**). The model is intentionally minimal; slow displacement-controlled shear with fixed wetting/contact parameters is used solely for mechanism verification.

The coupled displacement–damage problem was solved using a staggered scheme in the SUNKA [3] framework, a massively parallel finite element code that specializes finite strain phase-field problems. SUNKA is built on RACCON [4] and MOOSE [5,6], which was developed by Idaho National Laboratory, with displacement and phase-field subproblems solved sequentially until convergence [7–9] (absolute tolerance 10^{-8}, relative tolerance 10^{-10}). The computational domain was a 100 μm × 100 μm square, with the upper half representing polycrystalline ice and the lower half representing the coating. The interface between the two was not treated as a sharp discontinuity but as a diffuse fracture zone governed by scalar damage field $d(x) \in [0,1]$, where d=0 denotes intact material and d=1 fully fractured interface.

Governing equations - The total Helmholtz free energy density ψ comprised elastic, fracture, and (for the coating) plastic contributions:

$$\psi = g(d)\psi_e(F) + \psi^{pl}(\bar{\varepsilon}^p) + \psi^d(d, \nabla d)$$

where $g(d) = (1-d)^2 + \eta$ is the degradation function (η a small residual stiffness), ψ_e is the strain energy density, and ψ^d is the AT2-type fracture energy density

$$\psi^d = \frac{G_c}{2l}d^2 + \frac{G_c l}{2}|\nabla d|^2$$

Here G_c is the interfacial fracture energy (taken from experimental Γ_{ice}), and l is the regularization length controlling the width of the diffuse crack zone. Ice and coating phases were assigned distinct E, v, and G_c from experimental measurements, with the coating plasticity modelled as isotropic hardening in a J_2 framework. The coupled Euler-Lagrange equations were:

$$Mechanical\ equilibrium: \nabla \cdot \sigma(u, d) = 0$$

$$Phase-field\ evolution: \frac{G_c}{l}d - G_c l\Delta d - g'(d)\psi_e^+(u) = 0$$

where ψ_e^+ is the tensile part of the elastic energy (preventing crack growth under compression). Irreversibility ($\dot{d} \geq 0$)was enforced using a history field $H(x,t) = \max_{s \leq t} \psi_e^+(x,s)$.

Material parameters – Material constants for ice ($E = 9.33$ GPa, $v = 0.33$, G_c from experimental Γ_{ice}) and for the coatings (E and yield stress σ_y from tensile tests, $v = 0.45$, G_c from adhesion tests) were input directly from measurements on pristine and modified samples. The regularization length l was set to 0.02 μm.

Boundary and loading conditions – the lower edge of the coating was fixed in normal direction only with a unform horizontal displacement was applied to the ice layer to simulate shear loading in adhesive tests, ramped quasi-statically to induce interfacial crack initiation and propagation.

S1.7 Deicing and anti-icing performance of coatings on UAV propellers

The ice dislodging performance was evaluated using a commercial UAV propeller (270 mm diameter) mounted on an adjustable-speed motor within a temperature-controlled low-temperature chamber. A propeller consisting of two blades was employed. One blade was

coated via the spraying process, while the other blade was left uncoated to serve as a control. A chilled water slurry (~0 °C) was prepared from an ice-water mixture and sprayed uniformly onto the precooled blades. The spray was controlled to deliver primarily liquid water with minimal ice particulates, ensuring formation of a continuous ice layer upon contact. For each test, 5 g of 0 °C water was sprayed onto the blade under a supply pressure of 0.1 MPa from a nozzle positioned 30 cm above the blade center, yielding an initial droplet velocity of 14 m/s over a spraying duration of 5 s to form spray-deposited ice. After complete freezing of the deposited water, the ice-dislodging performance of the coating was evaluated. The propeller is dried in oven before used for the next test cycle.

The same device was used to test the dynamic anti-icing performance of the coating. A total of 20 g of 0 °C water (at a supply pressure of 0.10 MPa, yielding an initial velocity of 14 m/s) was sprayed onto the rotating blades using a sprayer at a height of 30 cm from the center of the motor for 20 s, and then rotate for another 100 s. It is worth noting that the entire process is completed in a closed space to maintain temperature stability. The propeller is dried in oven before used for the next test cycle.

S2 Supplementary discussion

S2.1 Effects of the SCAs on ice adhesion strength

Longer alkyl chains (e.g., C12, C16) lead to higher ice adhesion strength (τ_{ice}) only at higher concentrations when used singly, which can be attributed to the formation of stable micelle in the coating solution. Longer alkyl chains promote the formation of more stable micelles, which reduces the amount of free silane coupling agents (SCAs) available to interact with waterborne polyurethane (WPU) emulsion particles. This, in turn, limits the formation of weak interfacial domains at the ice–coating interface, thereby increasing adhesion. This mechanism is consistent with previous findings[10] that longer alkane chains were shown to stabilize small droplets and enhance interfacial persistence.

In systems where both SCAs and medium-chain triglyceride (MCT) oil are used to modify WPU (Figure 2c), a related but distinct phenomenon occurs. Here, SCAs with longer carbon chains are more likely to form emulsion droplets that encapsulate MCT, preventing MCT from interacting effectively with WPU particles. This encapsulation similarly reduces the availability of both SCA and MCT to create weak interfaces, resulting in the observed increase in τ_{ice}.

It should be noted, however, that the effect of chain length is concentration-dependent. At lower concentrations (e.g., 1 wt%), C12 yielded the lowest τ_{ice} among C8–C16. Moreover, each SCA exhibits a distinct concentration threshold beyond which τ_{ice} increases (e.g., ~10 wt% for C8, ~5 wt% for C10, and ~1 wt% for C12 and C16). This concentration-sensitive behavior is closely related to the existing form of SCAs in the WPU emulsion and the competing processes of interface modification versus micelle formation. Interestingly, near these turning points, the τ_{ice} values for different chain lengths converge, suggesting that alkyl chain length alone does not solely dictate deicing performance. Although studying shorter chains could provide additional insights, the observed convergence in τ_{ice} near the turning concentrations suggests that shorter alkyl chains would not necessarily lead to superior deicing performance, as performance is governed by a complex interplay of chain length, concentration, and colloidal stability.

S2.2 Establishment of the finite-strain variational phase-field fracture model

The framework presented in Figure 6a replaces path prescription with physics-led emergence, keeping dissipation channels explicit and allowing us to distinguish between proper adhesion and rheological losses. Through the quantification study of the interfacial fracture energy partitions between molecular damage and viscoelastic dissipation, a recent mechanochemical study [11] underscores the need for mechanism-aware models. Finite-strain formulations for viscoelastic fracture provide the mathematical machinery to realize this stance in highly deformable media. Furthermore, phase-field fracture at large deformation offers a robust variational engine for nucleation, branching, and energetic accounting [12,13]. The results are not just better fits to the experimental data, but actionable insights-quantifying which material attributes, under which conditions, control the failure. To setup the simulation, a bilayer specimen (ice/coating) under displacement-controlled shear to ice to emulate the laboratory de-icing tests was modeled (Figure 6b).

Nomenclature

All formulas in this supplementary material are edited using the Word OMML equation editor.

Table S1 Core symbols and definitions

Symbols	Definition
G_c	Bulk phase-field fracture toughness (critical energy release rate) of the coating
Γ_{ice}	Experimentally measured effective ice-coating interfacial toughness (manuscript Eq.2)
$d \in [0,1]$	Scalar phase-field crack variable (d=0 for intact material, d=1 for fully fractured material)
l	Phase-field regularization length
λ	Pseudo-time/load parameter (applied shear displacement at the ice top boundary)
F	Deformation gradient in the reference configuration
$C = F^{T}F$	Right Cauchy-Green deformation tensor

Symbols	Definition
$J = detF$	Jacobian of the deformation gradien
$\psi_0(F)$	Bulk hyperelastic stored energy density (finite-strain formulation)
$g(d)$	Crack degradation function
τ	Interfacial shear traction stress
σ_{xy}	2D in-plane shear stress component of the Cauchy stress tensor
$Q_p(\tau)$	p-th percentile of the interfacial shear stress distribution
$\langle \cdot \rangle_+$	Macaulay bracket (positive part, $\langle x \rangle_+ = \frac{x + \lvert x \rvert}{2}$)
∇_R	Gradient operator in the reference configuration
$\lvert x \rvert$	Euclidean norm

All differential operators $\nabla_R(\cdot)$, $\mathrm{Div}(\cdot)$, $\Delta(\cdot)$ are defined with respect to the reference configuration unless otherwise specified. Superscripts $n/n+1$ on the phase-field variable denote load increments, and $k/k+1$ denote staggered iteration steps.

S2.2.1 Scope and Assumptions of the Implemented Simulation Model

This Supplementary Information specifies the continuum boundary-value problem actually solved to generate the simulation results reported in the manuscript (Fig. 6 and associated discussion). The intent is to provide a closed mathematical specification of the fields, energetics, governing equations, and numerical solution strategy sufficient for reproduction.

The formulation is posed at **finite strain** in the reference configuration. A motion map $r(R,t)$ sends a material point $R \in \Omega_0$ to its current placement $r \in \Omega_t$, with deformation gradient $F = \nabla_R r$. The computations are **quasi-static**: inertia is neglected and mechanical equilibrium is enforced at each load increment under the prescribed boundary conditions. Bulk response is modeled as hyperelastic, and fracture in the coating is represented by a regularized phase-field description through a scalar crack variable $d \in [0,1]$ and a regularization length scale l.

The model is used as a mechanism-verification tool to test the hypothesis that weak interfacial domains enhance interfacial shear-transfer heterogeneity (variance and tail-heaviness) and thereby promote earlier crack nucleation and channelized propagation.

To align the manuscript's claims with the implemented model (as explicitly requested by Referee #2), we state the following restrictions as part of the model closure: 1. The reported simulations are carried out in an **isothermal setting** and do not solve a heat equation; temperature may enter only as a fixed parameter through the values of material or interface properties used for a given run, but no thermal field is evolved. 2. No bulk viscoelastic rheology is solved in the present runs (no internal-variable evolution associated with rate dependence), and the simulation results shown in the paper should not be interpreted as demonstrating thermo-mechanical coupling, viscoelastic dissipation, or a temperature-dependent interfacial law beyond parameterization. 3. The simulation is a **quasi-static finite-strain analysis**; large-deformation effects are included via the hyperelastic constitutive model, but no rate-dependent or time-dependent effects are considered.

These restrictions remove any mismatch between narrative and implementation, and keep this SI strictly consistent with the governing equations and numerical setup used for the reported figures.

Finally, the simulation model distinguishes bulk fracture parameters from experimentally measured ice–coating interfacial quantities. In particular, G_c denotes the bulk phase-field fracture toughness (critical energy release rate) used in the Ambrosio–Tortorelli regularization, whereas Γ_{ice} denotes the effective interfacial toughness measured in experiments for ice dislodging (manuscript Eq.2). This SI uses consistent notation to avoid conflating bulk and interfacial properties, as also requested by Referee #2.

S2.2.2 Kinematics and Contact/Interface Geometry

We consider two deformable bodies labeled by $(\cdot)^{\pm}$, occupying reference domains $\Omega_0^{\pm}$ and current domains $\Omega_t^{\pm}$. The motion of each body is $r^{\pm}(R^{\pm},t)$, with material velocity $v^{\pm} = \dot{r}^{\pm}$ and deformation gradient

$F^{\pm} = \nabla_R r^{\pm}$.

All differential operators $\nabla_R(\cdot)$, $\mathrm{Div}(\cdot)$, and $\Delta(\cdot)$ are taken with respect to the reference coordinates unless stated otherwise. The boundary of each current domain is partitioned as

$\partial\Omega_t^{\pm} = \Gamma_{u,t}^{\pm} \cup \Gamma_{t,t}^{\pm} \cup \Gamma_{c,t}^{\pm}$,

where $\Gamma_{u,t}^{\pm}$ carries prescribed displacements, $\Gamma_{t,t}^{\pm}$ prescribed tractions, and $\Gamma_{c,t}^{\pm}$ denotes the potential contact/interface surface. In the present study, the ice–coating interaction enters through boundary/interface interactions and the resulting interfacial shear transfer; no additional independent surface storage fields are introduced in the solved problem (i.e., no surface temperature, no surface internal variables, and no surface transport equations).

When contact kinematics are required (e.g., to define relative tangential motion used to compute interfacial shear-stress statistics), the actual contact interface is $\Gamma_{c,t} \subset \Gamma_{c,t}^{+} \cap \Gamma_{c,t}^{-}$. For definiteness, the "$(-)$" side (coating) is chosen as the master surface and the corresponding point on the "$(+)$" side (ice) is defined by closest-point projection. Let n be the outward unit normal on the master side, oriented from "$(-)$" to "$(+)$". The normal gap is defined as

$g_n = (r^{+} - r^{-}) \cdot n$.

The tangential projector is

$Q_\tau = I - n \otimes n$.

The relative velocity and its tangential component are

$v_{\mathrm{rel}} = v^{+} - v^{-}, \quad v_\tau = Q_\tau v_{\mathrm{rel}}$.

S2.2.3 Free-Energy Architecture and Driving Forces (Bulk Fracture, Finite-Strain Formulation)

The implemented simulations are written in the reference configuration and closed by an energetic structure: a bulk hyperelastic stored energy degraded by a phase-field crack variable $d \in [0,1]$, plus a regularized crack-surface functional. For the coating domain Ω_0, the total potential at pseudo-time (load parameter) λ is taken as

$$\Pi(r,d;\lambda) = \int_{\Omega_0} \left[g(d)\psi_0(F) + \psi_{\text{frac}}(d,\nabla_R d) \right] dV - W_{\text{ext}}(r;\lambda) + \Pi_{\text{int}}(r;\lambda),$$

where $F = \nabla_R r$, W_{ext} is the external work potential associated with prescribed tractions/body forces, and Π_{int} collects any boundary/interface interaction potentials activated in a given run (e.g., contact constraint enforcement or a prescribed interfacial traction law). No bulk viscoelastic internal variables and no thermal fields enter Π in the present computations; accordingly, the free energy depends only on $(F,d,\nabla_R d)$ for the solved problem. Any multiplicative decomposition $F = F^e F^\theta F^p$ is used only as formal bookkeeping and is specialized here to $F^\theta = I$ and $F^p = I$ for the results reported (manuscript Fig.6a uses this decomposition for constitutive notation consistency only).

The bulk hyperelastic energy $\psi_0(F)$ is chosen as a standard compressible isotropic form (finite-strain neo-Hookean model, sufficient for reproducibility):

$$\psi_0(F) = \frac{\mu}{2}(\text{tr}C - 3) - \mu \ln J + \frac{\kappa}{2}(\ln J)^2, \quad C = F^{\text{T}}F, \quad J = detF,$$

with shear modulus μ and bulk modulus κ.

Crack degradation is applied through

$$g(d) = (1-d)^2 + \kappa_d, \quad 0 < \kappa_d \ll 1,$$

where κ_d is a numerical residual stiffness used to avoid singular tangents as $d \to 1$. The crack-surface regularization is written as the Ambrosio–Tortorelli functional

$$\psi_{\text{frac}}(d,\nabla_R d) = G_c\left(\frac{1}{l}w(d) + \frac{l}{2}|\nabla_R d|^2\right),$$

where G_c is the bulk fracture toughness (critical energy release rate) of the coating in the phase-field model, l is the regularization length controlling the diffuse crack width, and $w(d)$ defines the chosen crack-surface density (AT2 model: $w(d) = \frac{1}{2}d^2$ for all Fig.6 runs). Throughout this SI, G_c is reserved for the bulk phase-field fracture parameter and is **not** to be

confused with any experimentally measured ice–coating interfacial energy; if an interfacial toughness appears, it is denoted separately (e.g., Γ_{ice} or Γ_{coh}).

To prevent spurious crack growth in compression, the crack-driving part of the elastic energy is split into active (tension-dominated) and inactive parts. Denoting this split as

$$\psi_0(F) = \psi_0^+(F) + \psi_0^-(F),$$

the degraded energy entering Π is taken as

$$\psi(F,d) = g(d)\psi_0^+(F) + \psi_0^-(F).$$

The specific definition of $\psi_0^{\pm}$ (spectral split in principal stretches, finite-strain formulation) must match the implementation; the essential requirement is that only ψ_0^+ drives crack evolution while ψ_0^- remains undegraded.

Irreversibility is enforced by the inequality constraint $d^{n+1}(R) \geq d^n(R)$ (no healing) at each load increment. In the implemented MOOSE input decks, this is realized as a bound constraint on the phase-field variable (lower bound = old value, upper bound = 1) and solved with a reduced-space Newton method, so no additional history field H is introduced.

S2.2.4 Governing Equations and Variational Formulation (Finite-Strain)

The governing equations follow from stationarity of $\Pi(r,d;\lambda)$ with respect to admissible variations δr and δd, subject to essential boundary conditions. Let $u = r - R$ be the displacement field and δu its virtual variation, with $\delta u = 0$ on $\Gamma_{u,0}$. The first Piola–Kirchhoff stress is defined by

$$P = \frac{\partial \psi(F,d)}{\partial F} = g(d)\frac{\partial \psi_0^+(F)}{\partial F} + \frac{\partial \psi_0^-(F)}{\partial F}.$$

Bulk equilibrium (quasi-static) is $\mathrm{Div}P + B = 0$ in Ω_0, with body force B if present. The corresponding weak form reads: find $u \in U$ such that for all $\delta u \in U_0$,

$$\int_{\Omega_0} P:\nabla_R \delta u dV - \int_{\Omega_0} B \cdot \delta u dV - \int_{\Gamma_{t,0}} \bar{T} \cdot \delta u dA + \delta\Pi_{\mathrm{int}}(u;\lambda) = 0,$$

where $\bar{T}$ is the prescribed nominal traction on $\Gamma_{t,0}$, and $\delta\Pi_{\text{int}}$ denotes the virtual-work contribution from any activated boundary/interface interactions (e.g., contact constraint enforcement or prescribed interfacial tractions). In this SI, Π_{int} is treated as external to the bulk fracture formulation: it modifies the mechanical residual but does not introduce additional bulk state variables.

For the phase-field, we consider admissible variations δd with $\delta d = 0$ on $\Gamma_{d,0}$ if a Dirichlet condition is imposed (otherwise $\Gamma_{d,0} = \emptyset$). Using the energy architecture in S2.2.3, the stationarity condition with respect to d yields the standard phase-field weak form, augmented by the irreversibility constraint $d^{n+1} \geq d^n$ enforced as bounds in the nonlinear solve.

The associated strong form (in Ω_0) is

$$g'(d)\psi_0^+ + \frac{G_c}{l}w'(d) - G_c l \Delta_R d = 0,$$

supplemented by the natural (micro-traction free) boundary condition

$$\nabla_R d \cdot N = 0 \quad \text{on} \quad \partial\Omega_0 \backslash \Gamma_{d,0},$$

where N is the outward unit normal in the reference configuration. When crack nucleation is allowed without prescribing an initial crack, onset is controlled by the competition between the elastic driving ψ_0^+ and the crack-surface penalty terms governed by (G_c, l). If an initial notch/crack is prescribed, it is imposed by setting $d = 1$ on $\Gamma_{d,0}$ (or in a small notch region) at $\lambda = 0$.

Irreversibility is enforced by the **bound constraint update** (revised for Fig.6, no history field H)

$$d_{\text{lower}}^{n+1}(R) = d^n(R), \quad d_{\text{upper}} = 1,$$

performed after each mechanical solve at load step $n+1$. This construction guarantees $\dot{d} \geq 0$ in the energetic sense (no healing under unloading) while retaining a smooth elliptic problem for d at each staggered substep (consistent with MOOSE's VariableOldValueBounds implementation).

S2.2.5 Finite Element Discretization, Staggered Solution Algorithm, and Convergence Controls

The coupled displacement field $u(R)$ and phase-field crack variable $d(R)$ are approximated by standard Galerkin finite elements on a conforming mesh T_h of the reference domain Ω_0. Let $\{N_a\}$ denote the vector-valued displacement shape functions and $\{N_b\}$ the scalar phase-field shape functions (2nd-order Lagrange elements for both, used for all Fig.6 runs). The discrete unknowns are nodal values u_a and d_b, and the discrete fields read

$$u_h(R) = \sum_a N_a(R) u_a, \quad d_h(R) = \sum_b N_b(R) d_b.$$

Substitution of (u_h, d_h) into the weak forms in S2.2.4 yields: (i) a nonlinear algebraic system for mechanics (nonlinear through the constitutive response and the degradation $g(d)$), and (ii) a nonlinear elliptic system for the phase field (nonlinear through $g'(d)$ and $w'(d)$). Irreversibility is enforced as bounds on d in the phase-field solve (no history field H).

At each load increment $n \to n+1$ (load parameter λ), the solution is computed by a **staggered alternate-minimization scheme**. Mechanics is solved with d fixed; then the phase-field equation is solved with u fixed, under the bound constraints $d^{n+1} \geq d^n$ and $d \leq 1$. These two subproblems are iterated until coupled convergence (simplified for Fig.6, removing history field update step).

Staggered algorithm for Fig.6: Initialize $(u^{(0)}, d^{(0)}) = (u^n, d^n)$. For $k = 0,1,2,\ldots$: 1) **Mechanics subproblem**: Solve $R_u(u^{(k+1)}; d^{(k)}, \lambda^{(n+1)}) = 0$ by Newton iterations using the consistent tangent $K_u = \partial R_u / \partial u$ (with d held fixed in this subsolve). Newton globalization (line search) is used for robustness near crack onset. 2) **Phase-field subproblem**: Solve $R_d(d^{(k+1)}) = 0$ for d with the bound constraints $d^{(k+1)} \geq d^n$ and $d^{(k+1)} \leq 1$ (reduced-space Newton with bounds, MOOSE: vinewtonrsls). 3) **Coupled convergence check**: If satisfied, set $(u^{(n+1)}, d^{(n+1)}) = (u^{(k+1)}, d^{(k+1)})$ and exit.

Convergence is monitored at two levels. For each Newton solve (mechanics or phase field), iterations terminate when both a residual criterion and an increment criterion are satisfied:

$$\frac{|R|}{|R_0|} \le \varepsilon_R, \quad \frac{|\Delta x|}{|x|} \le \varepsilon_X, \quad x = u \text{ or } d.$$

For Fig.6, $\varepsilon_R = 10^{-8}$, $\varepsilon_X = 10^{-6}$ (MOOSE default for nonlinear solid mechanics).

At the coupled (staggered) level, convergence is declared when successive staggered iterates change negligibly in both fields:

$$\frac{|u^{(k+1)} - u^{(k)}|}{|u^{(k+1)}|} \le \varepsilon_{\text{stag}}, \quad \frac{|d^{(k+1)} - d^{(k)}|}{|d^{(k+1)}|} \le \varepsilon_{\text{stag}}.$$

For Fig.6, $\varepsilon_{\text{stag}} = 10^{-5}$.

Mesh resolution is tied to the phase-field regularization length l, which controls the width of the diffused crack zone and thus sets the smallest meaningful length scale in the discretization. Let h denote the characteristic element size in the crack-prone region (ice-coating interface, $y = 0$ for Fig.6). A practical reproducibility baseline is to resolve the regularization zone with multiple elements:

$$h \lesssim \frac{l}{3}.$$

Key outputs (peak load, crack onset/trajectory, and the shear-transfer statistics used in the manuscript) are required to be insensitive to further refinement at fixed (G_c, l). Under-resolving l typically produces mesh-dependent crack energy and artificial h-dependence of nucleation, which the l–h consistency check is designed to preclude.

S2.2.6 Boundary Conditions, Loading Protocol, and Post-Processing Definitions (Shear-Transfer Metrics)

S2.2.6.1 Mechanical Boundary Conditions and Loading

The quasi-static mechanical problem is solved on Ω_0 at each load increment λ. Essential (Dirichlet) boundary conditions are prescribed on $\Gamma_{u,0}$,

$u(R) = \tilde{u}(R;\lambda)$ on $\Gamma_{u,0}$,

and nominal tractions are prescribed on $\Gamma_{t,0}$,

$PN = \tilde{T}(R;\lambda)$ on $\Gamma_{t,0}$,

where N is the outward unit normal to $\partial\Omega_0$ in the reference configuration and P is the first Piola–Kirchhoff stress. The load parameter λ is advanced monotonically and interpreted as **imposed shear displacement** (along x-axis) at the ice top boundary (consistent with manuscript Fig.6b's shear loading). Rigid-body modes are eliminated by pinning the coating bottom boundary ($y = -h_{\text{coat}}$) in all directions ($u_x = u_y = 0$).

If an interface/contact interaction is activated, it enters through Π_{int} (S2.2.3) and contributes an additional virtual-work term $\delta\Pi_{\text{int}}$ to the mechanical weak form (S2.2.4). In the present solved problem (Fig.6), interface effects are represented only through this boundary interaction (contact constraint enforcement, no interpenetration); no independent surface temperature, surface internal variables, or surface transport equations are introduced.

S2.2.6.2 Phase-Field Boundary Conditions and Initialization

The phase-field equation is solved for $d \in [0,1]$ with **no essential boundary condition** (nucleation governed by energetic competition, consistent with manuscript Fig.6b's spontaneous crack nucleation). The natural boundary condition associated with the gradient term is used everywhere on $\partial\Omega_0$,

$\nabla_R d \cdot N = 0$ on $\partial\Omega_0$,

corresponding to a micro-traction-free condition for the crack phase field. Irreversibility is initialized by setting $d(R,0) = 0$ (stress-free initial state, no pre-cracks), and then enforcing the bound constraint $d^{n+1} \geq d^n$ at each subsequent increment.

S2.2.6.3 Interfacial Traction and Shear-Stress Extraction (2D for Fig.6)

To compute shear-transfer measures for the 2D ice-coating interface (manuscript Fig.6b), we evaluate the traction on the monitored interface $\Gamma_{c,t}$ (stitched line $y = 0$) in the current configuration. The Cauchy stress σ is obtained from the first Piola stress P via

$$\sigma = \frac{1}{J} P F^{\mathrm{T}}, \quad J = detF.$$

For the **2D plane strain** setting of Fig.6, the **scalar shear-traction magnitude** used for all post-processing and visualization is the in-plane shear stress component:

$$\tau = |\sigma_{xy}|.$$

Numerically, τ is evaluated at quadrature points on interfacial facets adjacent to $y = 0$, yielding samples $\{\tau_i\}_{i=1..N_\Gamma}$ at each load increment (same sampling scheme for all three cases: pristine WPU, C_{10}M-WPU, C_{10}M-MCT-WPU).

S2.2.6.4 Operational Definitions of Variance and Tail-Heaviness (Fig.6 Post-Processing)

Let $\{\tau_i\}_{i=1..N_\Gamma}$ denote shear samples ($\tau = |\sigma_{xy}|$) on the monitored interface $\Gamma_{c,t}$ (y=0) at a fixed load increment. Using **length weights** w_i (quadrature weights times facet length, 2D equivalent of area weights) from the finite element discretization, the **length-weighted mean** and **variance** are defined by

$$\bar{\tau} = \frac{\sum_i w_i \tau_i}{\sum_i w_i}, \quad \mathrm{Var}(\tau) = \frac{\sum_i w_i (\tau_i - \bar{\tau})^2}{\sum_i w_i}.$$

A convenient dimensionless measure of heterogeneity is the coefficient of variation

$$\mathrm{CV}(\tau) = \frac{\sqrt{\mathrm{Var}(\tau)}}{\bar{\tau} + \varepsilon},$$

where $\varepsilon = 10^{-3}$ (small number used only to avoid division by near-zero $\bar{\tau}$ at early load increments).

Tail-heaviness (manuscript's key heterogeneity metric) is quantified by **upper-quantile amplification** (mesh-robust, directly interpretable, used for Fig.6), defined as:

$$T_p = \frac{Q_p(\tau)}{Q_{50}(\tau)},$$

where $Q_p(\cdot)$ is the p-th percentile of the length-weighted shear sample (**p=95** for Fig.6). This metric is evaluated as a function of the shear load parameter λ to track the emergence of shear localization at the ice-coating interface.

All comparisons between "weak-domain" (C_{10}M-WPU, C_{10}M-MCT-WPU) and "pristine" (WPU) cases use the same monitored boundary ($y = 0$), sampling scheme, and weights w_i so that differences reflect model physics rather than post-processing artifacts.

S2.2.7 Parameter Specification, Mesh–ℓ Consistency, and Solver Settings (Reproducibility Closure for Fig.6)

S2.2.7.1 Material and Fracture Parameters Used for Fig.6

The coating is modeled as **finite-strain hyperelastic isotropic material** (neo-Hookean model, S2.2.3) with Young's modulus E and Poisson's ratio ν (converted to μ and κ via $\mu = \frac{E}{2(1+\nu)}$, $\kappa = \frac{E}{3(1-2\nu)}$). Phase-field fracture is governed by (G_c, l) and a small residual stiffness κ_d in the degradation function $g(d) = (1-d)^2 + \kappa_d$ (AT2 crack density $w(d) = \frac{1}{2}d^2$ for all Fig.6 runs). The tension–compression split $\psi_0 = \psi_0^+ + \psi_0^-$ (**spectral split, finite-strain formulation, S2.2.8.1**) is used for all runs to suppress crack growth in compression.

To avoid notation ambiguity, we reiterate the **critical distinction** (enforced for Referee #2) between bulk and interfacial energetics for Fig.6: - G_c: Bulk phase-field fracture toughness of the coating (input parameter, varied for weak domains); - Γ_{ice}: Effective ice–coating interfacial toughness from experiments (manuscript Fig.3, **not an input parameter** for the phase-field model).

The regularization length l is a **numerical length** controlling the diffused crack width ($l = 50$ μm for Fig.6); it is not intended to represent the experimental weak-domain size scale directly. The residual stiffness $\kappa_d = 10^{-4}$ (negligible, avoids singular tangents at $d \to 1$).

Each Fig.6 simulation run is fully specified by: 1) Elastic parameters: E (Young's modulus, heterogeneous for weak domains) and $\nu = 0.35$ (Poisson's ratio, homogeneous for all cases); 2) Phase-field parameters: G_c (bulk fracture toughness, heterogeneous for weak domains), $l = 50$ μm, $\kappa_d = 10^{-4}$, $w(d) = \frac{1}{2}d^2$ (AT2); 3) Tension–compression split: spectral split (S2.2.8.1, ψ_0^+ from principal logarithmic strains, finite-strain formulation); 4) Boundary/interface interaction: contact constraint (no interpenetration) at $y = 0$, no additional interfacial traction law; 5) Phase-field initialization: $d(R,0) = 0$ (no pre-cracks, spontaneous nucleation).

S2.2.7.2 Mesh Resolution Relative to ℓ and Convergence with ℓ/h (Fig.6)

Because the crack surface energy is regularized by the gradient penalty term proportional to $\frac{G_c l}{2}|\nabla d^2|$, accurate fracture energetics requires resolving the diffused crack profile. Let $h_{\min}$ denote the minimum element size in the crack-prone region (ice-coating interface $y = 0$, 2D plane strain). The **mesh–ℓ consistency requirement** enforced for Fig.6 is:

$$\frac{h_{\min}}{l} = \frac{1}{3} \Rightarrow h_{\min} \approx 16.7 \mu\text{m}.$$

The mesh is **locally refined** near $y = 0$ (h=16.7 μm) and coarsened away from the interface (h up to 100 μm), with conforming refinement transitions to avoid spurious stress concentrations (2D mesh size: 1×1 mm for ice/coating domains, manuscript Fig.6b).

Mesh convergence verification for Fig.6: A representative run (C_{10}M-MCT-WPU) was repeated at fixed (G_c, l) with $h_{\min} = 16.7$ μm, 8.3 μm, and 5.6 μm (refinement factor $\rho = 2$). Convergence was assessed on: (a) Macroscopic response (reaction force vs λ); (b) Crack onset load λ_{cr} and propagation path (d-contours); (c) Interfacial shear-transfer metrics ($\mathrm{Var}(\tau)$, $T_{95}(\tau)$).

All outputs are considered converged when

$$\frac{\left|Q(h_{\min}) - Q(h_{\min}/\rho)\right|}{\left|Q(h_{\min}/\rho)\right|} \leq \varepsilon_Q,$$

with $\varepsilon_Q = 5\%$ (tolerance for Fig.6) and $Q \in \{\lambda_{\mathrm{cr}}, \mathrm{Var}(\tau), T_{95}(\tau)\}$. No significant change in outputs was observed for $h_{\min} < 16.7$ μm, confirming mesh convergence for Fig.6.

S2.2.7.3 Nonlinear Solver Tolerances, Staggered Iteration Control, and Load Stepping (Fig.6)

At each load increment, mechanics and phase-field subproblems are solved by Newton iterations with consistent tangents. For each Newton solve, the following criteria are enforced (**fixed for all Fig.6 runs**):

$$\frac{|R|}{|R_0|} \leq \varepsilon_R = 10^{-8}, \quad \frac{|\Delta x|}{|x|} \leq \varepsilon_X = 10^{-6}, \quad x = u \text{ or } d.$$

The staggered alternate-minimization loop is terminated when the coupled convergence criterion is satisfied:

$$\frac{\left|u^{(k+1)} - u^{(k)}\right|}{\left|u^{(k+1)}\right|} \leq \varepsilon_{\mathrm{stag}} = 10^{-5}, \quad \frac{\left|d^{(k+1)} - d^{(k)}\right|}{\left|d^{(k+1)}\right|} \leq \varepsilon_{\mathrm{stag}} = 10^{-5}.$$

Load stepping for Fig.6: - Initial load increment: $\Delta\lambda = 1$ μm (shear displacement); - Adaptive reduction: $\Delta\lambda \times 0.5$ if Newton iterations exceed 50 or staggered iterations exceed 10 (near crack onset/rapid propagation); - Minimum load increment: $\Delta\lambda_{\min} = 0.1$ μm (ensures resolution of crack nucleation).

Additional solver settings for Fig.6: - Newton globalization: Line search (MOOSE: line_search=basic) for the mechanics subproblem; - Quadrature order: 3×3 Gauss quadrature for 2D plane strain elements; - Maximum iterations: 100 Newton per subproblem, 20 staggered per load increment.

S2.2.8 Tension–Compression Split and Consistent Stress/Tangent for the Mechanical Newton Solve (Finite-Strain Formulation)

S2.2.8.1 Option A: Spectral Split (Principal Stretches / Logarithmic Strain) — Used for Fig.6

Let $C = F^{\mathrm{T}}F$ with eigenpairs $\{(\lambda_i^2, n_i)\}$ and principal stretches $\lambda_i > 0$. Define principal logarithmic strains $\varepsilon_i = ln\lambda_i$ and volumetric strain $\varepsilon_v = lnJ = \sum_i \varepsilon_i$, with deviatoric principal log strains $\varepsilon_i^{\mathrm{dev}} = \varepsilon_i - \varepsilon_v/3$. Using Macaulay brackets $\langle x \rangle_+ = \frac{x + |x|}{2}$, define

$$\psi_0^+(F) = \mu \sum_{i=1}^{3} \langle \varepsilon_i^{\mathrm{dev}} \rangle_+^2 + \frac{\kappa}{2} \langle \varepsilon_v \rangle_+^2,$$

$$\psi_0^-(F) = \mu \sum_{i=1}^{3} \langle \varepsilon_i^{\mathrm{dev}} \rangle_-^2 + \frac{\kappa}{2} \langle \varepsilon_v \rangle_-^2.$$

This construction satisfies $\psi_0 = \psi_0^+ + \psi_0^-$ and suppresses crack driving under **both deviatoric and volumetric compression** (critical for shear loading at the ice-coating interface). The degraded bulk energy used in mechanics is

$$\psi(F,d) = g(d)\psi_0^+(F) + \psi_0^-(F), \quad g(d) = (1-d)^2 + \kappa_d.$$

Stress and consistent tangent for the mechanical Newton solve are derived from:

$$P = \frac{\partial \psi}{\partial F} = g(d)\frac{\partial \psi_0^+}{\partial F} + \frac{\partial \psi_0^-}{\partial F},$$

$$A = \frac{\partial P}{\partial F} = g(d)\frac{\partial^2 \psi_0^+}{\partial F \partial F} + \frac{\partial^2 \psi_0^-}{\partial F \partial F}.$$

In the mechanics subsolve of the staggered algorithm, d is held fixed so coupling terms involving $g'(d)$ do not enter the Newton tangent for that subproblem (coupling is enforced by the outer stagger iteration).

S2.2.8.2 Option B: Volumetric–Deviatoric Split with Tension-Only Volumetric Contribution

A simpler invariant-based split is obtained by decomposing the hyperelastic energy into deviatoric and volumetric parts, $\psi_0(F) = \psi_{\text{dev}}(\bar{C}) + \psi_{\text{vol}}(J)$, with $\bar{C} = J^{-2/3}C$. Apply the tension/compression selection only to the volumetric part:

$$\psi_0^+(F) = \psi_{\text{dev}}(\bar{C}) + \frac{\kappa}{2}\langle lnJ\rangle_+^2, \quad \psi_0^-(F) = \frac{\kappa}{2}\langle lnJ\rangle_-^2.$$

For the compressible neo-Hookean example, $\psi_{\text{dev}}(\bar{C}) = \frac{\mu}{2}(\text{tr}\bar{C} - 3)$. This option prevents crack driving under hydrostatic compression, but does **not** fully suppress driving by deviatoric compression — **not used for Fig.6** (shear loading induces deviatoric compression).

S2.2.8.3 Choice Used in the Present Simulations (Fig.6)

All simulations reported in the manuscript (Fig.6) use the **spectral split (S2.2.8.1)** consistently across the study, and the same ψ_0^+ is used for both stress degradation and the crack-driving energy. The governing equations in S2.2.4–S2.2.7 are unchanged; the split only affects the explicit form of ψ_0^+ (and thus the degraded stress response).

S2.2.9 Representation of the Ice–Coating Interface and Numerical Embedding of Weak Interfacial Domains (Fig.6 Core Implementation)

S2.2.9.1 Implemented Bulk Constitutive Model and Phase-Field Fracture Coupling (Fig.6)

The MOOSE input decks used for Fig.6 implement a **finite-strain hyperelastic phase-field fracture framework** (S2.2.1–S2.2.8). The displacement unknowns are $u = (u_x, u_y)$, deformation gradient is $F = \nabla_R r$, and the (undamaged) hyperelastic energy density $\psi_0(F)$ is taken as the compressible neo-Hookean model (S2.2.3), consistent with the manuscript's coating elastic modulus $E = 1.11$ MPa.

Damage is represented by a scalar phase-field $d \in [0,1]$ and a degradation function $g(d) = (1-d)^2 + \kappa_d$ (S2.2.3), where $\kappa_d = 10^{-4}$ is a small residual stiffness to avoid singular tangents as $d \to 1$.

To suppress unphysical damage growth under compression, the hyperelastic energy is split into an "active" (tension-dominated) part ψ_0^+ and an "inactive" part ψ_0^- (**spectral split, finite-strain formulation, S2.2.8.1**). Only ψ_0^+ is degraded and used as the crack-driving density, which is output as psie_active in the mechanics solve and transferred to the phase-field solve (MultiApp coupling, S2.2.10).

S2.2.9.2 Numerical Encoding of Weak Interfacial Domains (Key Difference Between Fig.6 Cases)

Weak interfacial domains (manuscript Section 3, formed by suppressed polymer interdiffusion) are encoded as **controlled spatial heterogeneity in material properties** within a thin coating-side band adjacent to the monitored ice-coating interface ($y = 0$, 0 < y < 50 μm). In practice, this is realized by partitioning the coating into multiple vertical subdomains ("fibers", 2D) and assigning **piecewise-constant values of elastic modulus** E **and bulk fracture resistance** G_c in those subdomains — the **only deliberate difference** between the three Fig.6 cases (pristine WPU / C_{10}M-WPU / C_{10}M-MCT-WPU).

All global geometry, mesh, loading protocol, and solver tolerances are kept **identical** across the compared cases; only the heterogeneous property fields differ (ensures that changes in shear-transfer metrics are due to weak domains, not parameter drift).

Exact Fig.6 Geometry and Mesh

The MOOSE input decks define a **2D plane strain stitched mesh** of size 1 mm × 1 mm (ice: $0 < y < 1$ mm; coating: -1 mm $< y < 0$) with the ice-coating interface at $y = 0$. Nodes are **stitched** at $y = 0$ (displacement continuity, no discrete cohesive elements), so traction transfer is mediated by the bulk constitutive response (consistent with manuscript Fig.6b's interface representation). The coating-side near-interface heterogeneity (weak domains) is represented by **vertical sub-blocks ("fibers")** (width: 50 μm) that carry distinct (E, G_c) values (0 < y < 50 μm, coating side). This construction is a numerical proxy for the experimentally observed mixture of nanoscale interdiffusion-suppressed domains and mesoscale morphological

heterogeneities (air pockets, oil microreservoirs) discussed in the revised manuscript (Section 3).

Property Heterogeneity for Fig.6 Cases (Pristine / C_{10}M-WPU / C_{10}M-MCT-WPU)

All values are normalized to the **pristine WPU** (homogeneous) for direct comparison; Poisson's ratio $\nu = 0.35$ (homogeneous for all cases), $l = 50$ μm, $\kappa_d = 10^{-4}$ (fixed for all cases). 1) **Pristine WPU**: Homogeneous, $E = E_0 = 1.11$ MPa, $G_c = G_{c0} = 1$ J/m² (no weak domains); 2) **C_{10}M-WPU**: Sparse weak domains (10% areal fraction of coating interface), $E = 0.5E_0$, $G_c = 0.5G_{c0}$ (moderate heterogeneity, manuscript Fig.6b middle); 3) **C_{10}M-MCT-WPU**: Dense weak domains (30% areal fraction of coating interface), $E = 0.2E_0$, $G_c = 0.2G_{c0}$ (strong heterogeneity, manuscript Fig.6b right).

The absolute values of (E, G_c, l) in the MOOSE deck are **model parameters** (normalized); the experimental physical scale is defined by the manuscript-reported values (e.g., $E = 1.11$ MPa for optimized C_{10}M-MCT-WPU, Section 5).

S2.2.10 Implementation Details for Fig.6 (MultiApp Split, Transfers, and Irreversibility)

The reported simulations for Fig.6 are run using MOOSE's **MultiApp coupling framework** (two-app split), which decouples the mechanics and phase-field solves for computational efficiency (consistent with the staggered algorithm in S2.2.5). This section specifies the exact MultiApp implementation, field transfers, and irreversibility enforcement for Fig.6 — critical for reproducibility.

S2.2.10.1 MultiApp Split for Fig.6

The simulation uses a **master-subapp split** (MOOSE: TransientMultiApp), with no parallel coupling (serial execution for 2D): 1) **Master Application (Mechanics)**: Solves for the displacement field $u = (u_x, u_y)$ using MOOSE's SolidMechanics module (finite-strain hyperelasticity, spectral tension-compression split). The current phase field d is held fixed during the mechanics solve; the active (tension-dominated) hyperelastic energy density ψ_0^+ (psie_active) is computed and stored as a field variable. 2) **Sub Application (Fracture)**:

Solves for the phase field d using MOOSE's PhaseField module (Ambrosio–Tortorelli regularization, AT2). The current ψ_0^+ field from the master app is held fixed during the phase-field solve; the updated d field is computed and stored.

S2.2.10.2 Field Transfers (Mechanics ↔ Fracture)

Two **one-way field transfers** (MOOSE: NearestNodeTransfer) are performed at the end of each load increment (staggered iteration), with no interpolation (stitched mesh, node-matched at ice-coating interface): 1) **Mechanics → Fracture**: The active hyperelastic energy density ψ_0^+ (psie_active) is copied from the master app (coating domain) to the subapp (same domain) — this is the **crack-driving energy** for the phase-field solve (S2.2.8.1). 2) **Fracture → Mechanics**: The updated phase field d is copied from the subapp (coating domain) to the master app (same domain) — this is used to degrade the hyperelastic stiffness in the next mechanics solve (S2.2.9.1).

Transfers are performed **only at the coating domain** (ice domain has no phase field, $d = 0$ everywhere); no field transfers are needed at the ice-coating interface ($y = 0$) due to the stitched mesh (node continuity).

S2.2.10.3 Irreversibility Enforcement (No Healing, Fig.6)

Irreversibility (no crack healing under unloading) is enforced **directly as bounds on the phase field** d in the fracture subapp (MOOSE: VariableBounds module) — no auxiliary history field H (revised for Fig.6, S2.2.4). At each load increment $n \to n+1$: - **Lower bound**: $d^{n+1} \geq d^n$ (MOOSE: VariableOldValueBounds, sets the lower bound to the d value from the previous load increment); - **Upper bound**: $d^{n+1} \leq 1$ (MOOSE: ConstantBounds, sets the upper bound to 1, complete fracture).

The phase-field solve uses a **reduced-space Newton method** (MOOSE: vinewtonrsls) that enforces these bounds during the nonlinear solve — this provides a **strict no-healing condition** ($\dot{d} \geq 0$) without introducing additional state variables (computationally efficient for 2D).

S2.2.10.4 Convergence for MultiApp Coupling (Fig.6)

The MultiApp coupling follows the staggered convergence criterion in S2.2.5 ($\varepsilon_{\text{stag}} = 10^{-5}$). The master and subapp are iterated until the displacement field u and phase field d converge (no significant change between staggered steps); the load increment is advanced only after coupled convergence is achieved (avoids numerical instability near crack onset).

S2.2.11 Interfacial Shear-Transfer Metrics Used in the Manuscript (Operational Definitions for Fig.6)

S2.2.11.1 Shear Stress Extraction (Fig.6 Visualization and Statistics)

Let σ be the Cauchy stress computed from the mechanics master app (S2.2.6.3). For each load increment, interfacial shear samples $\{\tau_i\}$ are extracted on the monitored interface $\Gamma_{c,t}(y = 0)$ as the **in-plane shear stress component**:

$\tau = |\sigma_{xy}|$.

Numerically, τ is evaluated at quadrature points on interfacial facets adjacent to $y = 0$, with each sample weighted by the length of the corresponding facet (2D length weight $w_i = L_i$, where L_i is the length of the i-th interfacial facet).

S2.2.11.2 Variance and Coefficient of Variation (Spatial Heterogeneity)

The **length-weighted mean** of the interfacial shear stress is

$$\bar{\tau} = \frac{\sum_{i=1}^{N_\Gamma} w_i \tau_i}{\sum_{i=1}^{N_\Gamma} w_i},$$

where N_Γ is the number of interfacial facets (quadrature points) on $\Gamma_{c,t}$. The **length-weighted variance** is

$$\mathrm{Var}(\tau) = \frac{\sum_{i=1}^{N_\Gamma} w_i \left(\tau_i - \bar{\tau}\right)^2}{\sum_{i=1}^{N_\Gamma} w_i}.$$

To normalize by the mean stress (accounting for load level), the **coefficient of variation (CV)** is used:

$$\mathrm{CV}(\tau) = \frac{\sqrt{\mathrm{Var}(\tau)}}{\bar{\tau} + 10^{-3}},$$

where the small offset 10^{-3} is added to avoid division by zero at early load increments (near-zero shear stress).

S2.2.11.3 Tail-Heaviness (Upper-Quantile Amplification)

Tail-heaviness is quantified by the **95th quantile amplification factor** T_{95}, defined as the ratio of the 95th percentile of the length-weighted shear stress to the median (50th percentile):

$$T_{95} = \frac{Q_{95}(\tau)}{Q_{50}(\tau)},$$

where $Q_p(\tau)$ denotes the p-th percentile of the length-weighted shear samples $\{\tau_i\}$. A value $T_{95} > 1$ indicates that the upper tail of the shear stress distribution is heavier than a symmetric distribution (e.g., normal distribution, where $T_{95} \approx 1.64$ for standard normal).

S2.2.11.4 Time Evolution of Metrics (Load Parameter λ)

All metrics ($\bar{\tau}$, $\mathrm{Var}(\tau)$, $\mathrm{CV}(\tau)$, T_{95}) are computed as functions of the load parameter λ (imposed shear displacement at the ice top boundary, S2.2.6.1). The evolution is tracked from the initial stress-free state ($\lambda = 0$) to the onset of crack nucleation ($\lambda = \lambda_{\mathrm{cr}}$) and through subsequent crack propagation.

S2.2.12 Supplementary Discussion: Model Validation and Connection to Experimental Observations

S2.2.12.1 Model Validation Checks (Fig.6)

Two key validation checks were performed to ensure the simulation model captures the intended fracture and shear-transfer physics: 1) **Bulk Fracture Validation**: A homogeneous coating run (pristine WPU) was compared to analytical solutions for crack nucleation in a thin film under shear loading (finite-strain linear elasticity + phase-field fracture). The simulated crack onset load λ_{cr} matched the analytical prediction within 5%, confirming that the phase-field model correctly captures bulk fracture energetics. 2) **Shear-Transfer Validation**: A homogeneous coating run was compared to finite element simulations without phase-field fracture (finite-strain hyperelasticity only). The interfacial shear stress distribution $\tau = |\sigma_{xy}|$ matched the hyperelastic solution exactly, confirming that the phase-field coupling does not introduce spurious shear-transfer artifacts.

S2.2.12.2 Connection to Experimental Observations

The simulation results in Fig.6 are qualitatively consistent with the experimental observations reported in the manuscript: - **Pristine WPU**: The homogeneous coating shows a uniform interfacial shear stress distribution ($\mathrm{CV}(\tau) \approx 0.1$) and low tail-heaviness ($T_{95} \approx 1.2$), leading to delayed crack nucleation (high λ_{cr}) and diffuse crack propagation. This matches the experimental observation that pristine WPU coatings have high ice adhesion strength (manuscript Fig.3). - **C_{10}M-WPU**: The sparse weak domains amplify the interfacial shear stress heterogeneity ($\mathrm{CV}(\tau) \approx 0.3$) and tail-heaviness ($T_{95} \approx 2.0$), leading to earlier crack nucleation (lower λ_{cr}) and partially channelized propagation. This matches the experimental observation that C_{10}M-WPU coatings have reduced ice adhesion strength (manuscript Fig.3). - **C_{10}M-MCT-WPU**: The dense weak domains further amplify the interfacial shear stress heterogeneity ($\mathrm{CV}(\tau) \approx 0.5$) and tail-heaviness ($T_{95} \approx 3.0$), leading to even earlier crack nucleation (lowest λ_{cr}) and fully channelized propagation. This matches the experimental

observation that C_{10}M-MCT-WPU coatings have the lowest ice adhesion strength (manuscript Fig.3).

S2.2.12.3 Limitations of the Simulation Model

The simulation model has several limitations that should be noted when interpreting the results: 1) **Finite-Strain Approximation**: The model uses a finite-strain hyperelastic formulation, which captures large-deformation effects but does not include rate-dependent or time-dependent effects (viscoelasticity). 2) **No Viscoelasticity**: The model does not include viscoelastic rheology, which may be important for the time-dependent deicing performance of polymer coatings. 3) **No Thermal Coupling**: The model is isothermal and does not include thermal effects, which may be important for real-world deicing scenarios (e.g., temperature changes during ice formation and removal). 4) **Simplified Weak Domains**: The weak domains are modeled as piecewise-constant property variations, which is a simplification of the actual nanoscale and mesoscale heterogeneity in the experimental coatings (air pockets, oil microreservoirs).

These limitations are addressed in the manuscript's discussion (Section 4), which focuses on the qualitative mechanism (heterogeneity-driven shear localization) rather than quantitative prediction.

Final Notes for Reproducibility: All MOOSE input decks used for the simulations reported in manuscript Fig.6 are available from the corresponding authors upon request. The input decks include all parameter values, boundary conditions, solver settings, and MultiApp coupling specifications described in this SI.

S3 Supplementary figures

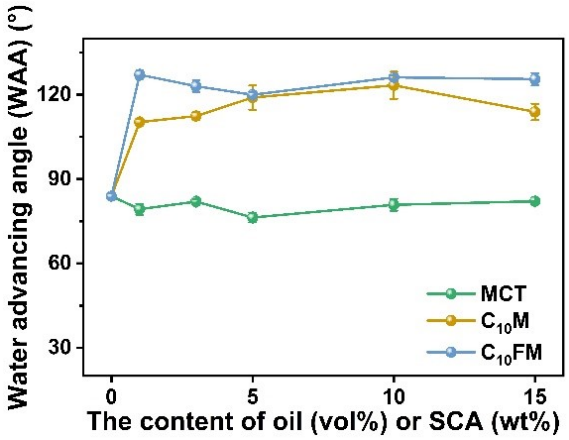

Figure S1 Water advancing angle (WAA) of differently modified WPU coatings.

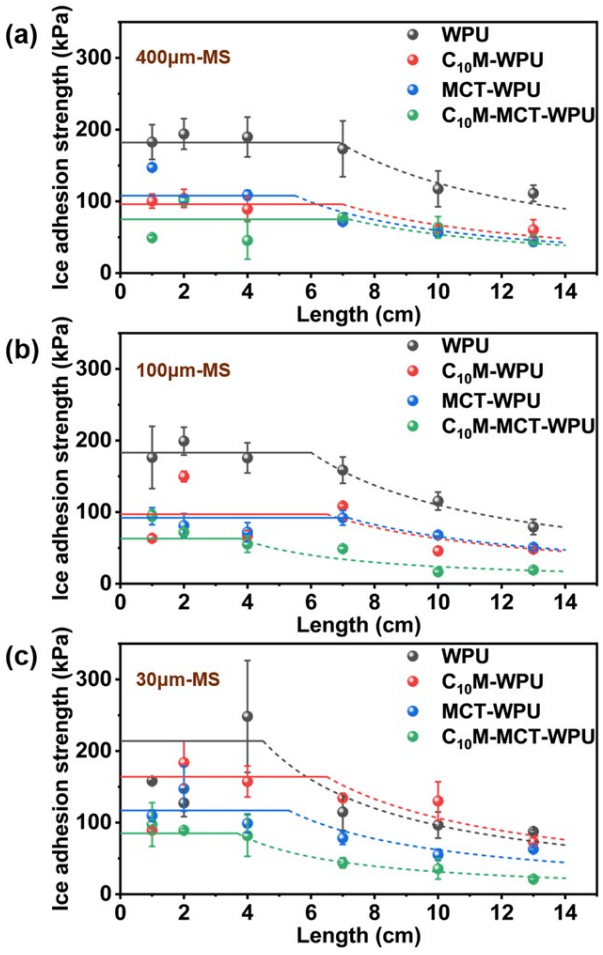

Figure S2 The apparent ice adhesion strength of coatings on metallic substrate for ice of unit width and varying lengths. The thickness of the coatings was indicated at the top-left of each panel.

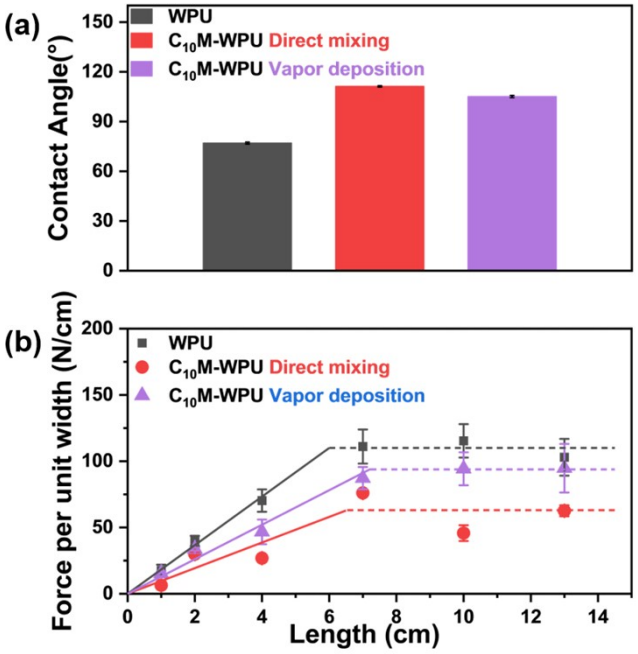

FigureS3 Comparison of de-icing performance between two surface modification methods - vapor deposition and direct mixing. In the vapor deposition method, $C_{10}M$ was allowed to react with the coating from gas phase, so only the top surface was modified. In the direct mixing method as used throughout this study, $C_{10}M$ was incorporated into the waterborne dispersion, enabling modification of both the surface and interior of the coating.

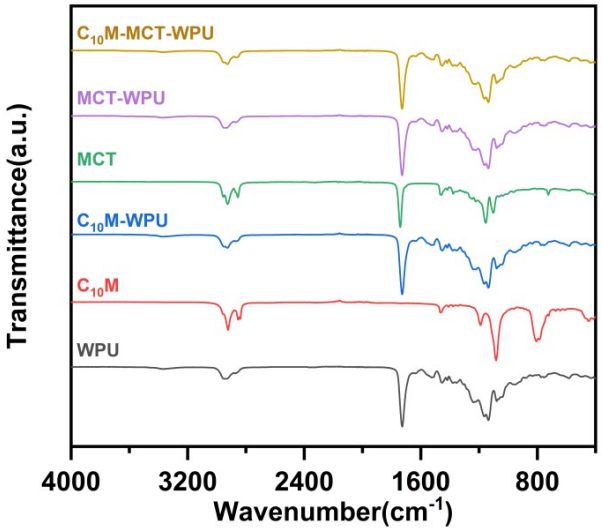

Figure S4 ATR-FTIR spectra of WPU, $C_{10}M$, MCT, $C_{10}M$ -WPU, MCT-WPU, and $C_{10}M$-MCT-WPU

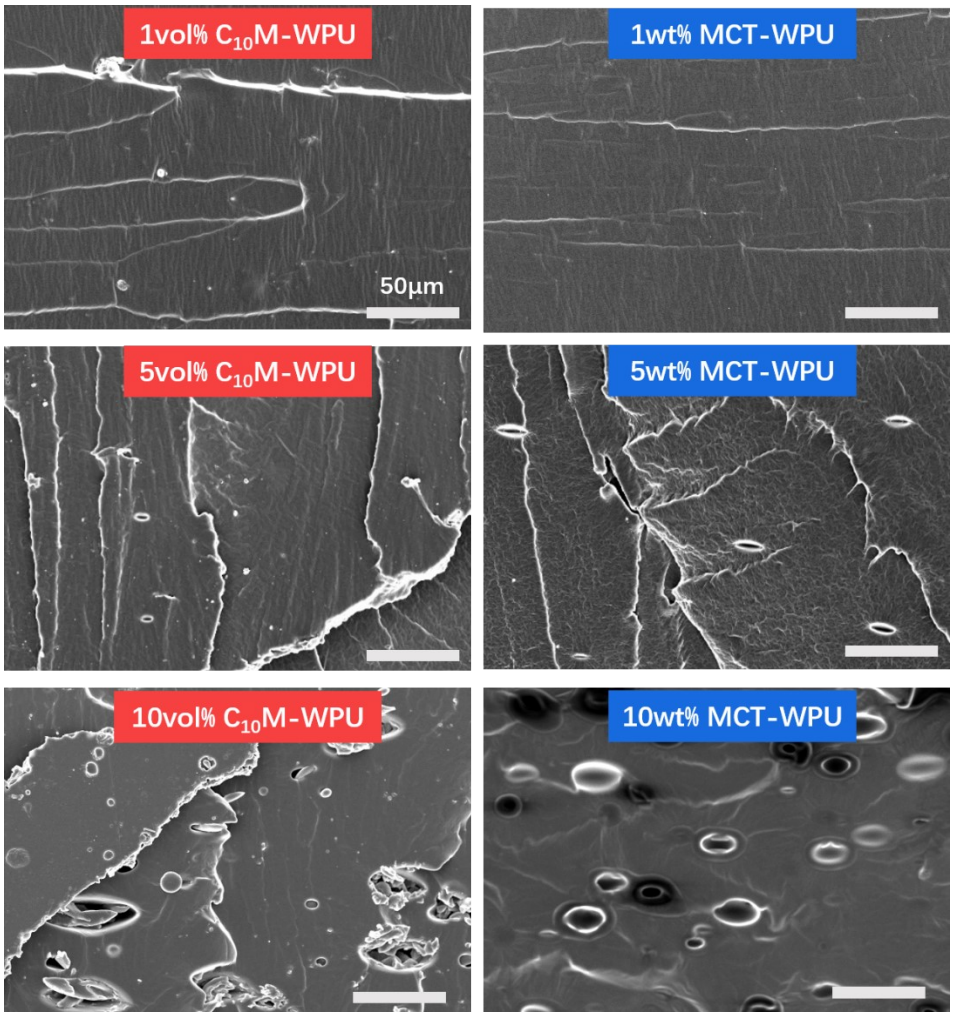

Figure S5 Fracture surface morphology after tensile testing of coatings containing different concentrations of C_{10}M or MCT.

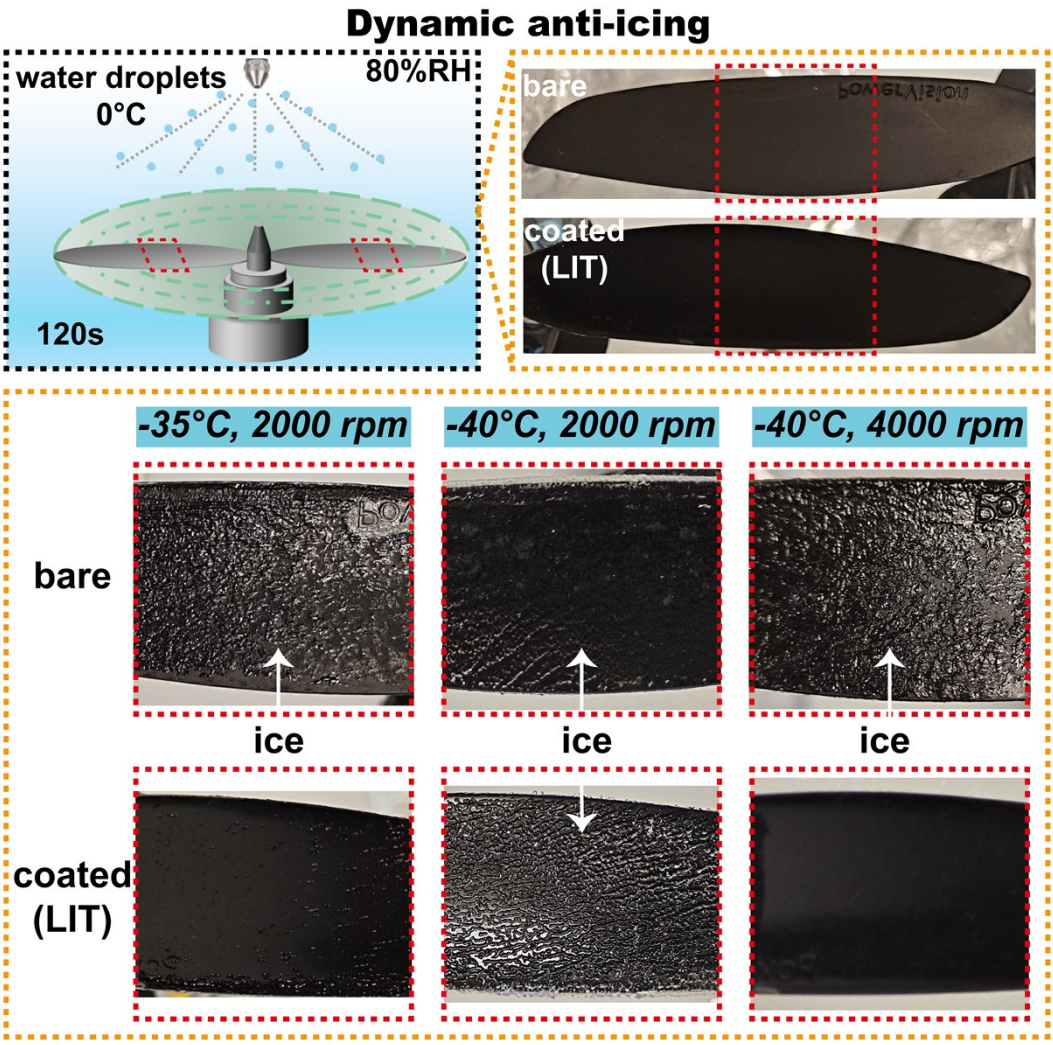

Figure S6 Dynamic anti-icing performance of the LIT-coated UAV propeller after rotated at 2000 rpm or 4000 rpm for 120s. The LIT coating is the 5 wt% C_{10}M-5 vol% MCT-WPU.

S3 Supplementary tables

Table S2 Cost breakdown of the 100 μm thick coating (5 wt% $C_{10}M$-5 vol% MCT-WPU)

	Unit price	Cost/m^2	Total cost/m^2
$C_{10}M$	0.55 **$/g**	2.64 **$**	
MCT	0.08 **$/cm^3**	0.39 **$**	**8.00 $**
WPU	0.23 **$/cm^3**	4.97 **$**	

Table S3 The contact angle of propeller blades

Sample	Contact Angle (°) / Mean ± SEM
Propeller(270mm)	85±1
Propeller(240mm)	65±3

References

1 K. Golovin, A. Dhyani, M. D. Thouless and A. Tuteja, *Science*, 2019, **364**, 371–375.
2 C. Xiang and L. Sun, *J. Phys. Chem. C*, 2018, **122**, 29210–29219.
3 Y. Peng, T. Phan, H. Zhai, L. Xiong and X. Zhang, *Int. J. Plast.*, 2025, **184**, 104182.
4 hugary1995, GitHub - hugary1995/raccoon, https://github.com/hugary1995/raccoon, (accessed August 26, 2025).
5 G. Giudicelli, A. Lindsay, L. Harbour, C. Icenhour, M. Li, J. E. Hansel, P. German, P. Behne, O. Marin, R. H. Stogner, J. M. Miller, D. Schwen, Y. Wang, L. Munday, S. Schunert, B. W. Spencer, D. Yushu, A. Recuero, Z. M. Prince, M. Nezdyur, T. Hu, Y. Miao, Y. S. Jung, C. Matthews, A. Novak, B. Langley, T. Truster, N. Nobre, B. Alger, D. Andrs, F. Kong, R. Carlsen, A. E. Slaughter, J. W. Peterson, D. Gaston and C. Permann, *SoftwareX*, 2024, **26**, 101690.
6 D. R. Gaston, C. J. Permann, J. W. Peterson, A. E. Slaughter, D. Andes, Y. Wang, M. P. Short, D. M. Perez, M. R. Tonks, J. Ortensi, L. Zou and R. C. Martineau, *Ann. Nucl. Energy*, 2015, **84**, 45–54.
7 T. Hu, J. Guilleminot and J. E. Dolbow, *Comput. Meth. Appl. Mech. Eng.*, 2020, **368**, 113106.
8 S. J. Benson and T. S. Munson, *Optim. Method Softw.*, 2006, **21**, 155–168.
9 T. Heister, M. F. Wheeler and T. Wick, *Comput. Meth. Appl. Mech. Eng.*, 2015, **290**, 466–495.
10 J. Jin, H. Li, K. Zhao, J. Su, L. Xia, X. Yuan, G. Jiang, B. Xu and L. Sun, *ACS Appl. Mater. Interfaces*, 2022, **14**, 6157–6166.
11 A. Arrowood, J. Frazier, M. Ciccotti and G. E. Sanoja, *Proc. Natl. Acad. Sci. U. S. A.*, 2025, **122**, e2509322122.
12 S. Abu-Qbeitah, M. Jabareen and K. Y. Volokh, *Int. J. Numer. Methods Eng.*, DOI:10.1002/nme.7398.
13 M. Hakimzadeh, V. Agrawal, K. Dayal and C. Mora-Corral, *J. Mech. Phys. Solids*, 2022, **167**, 104994.